

Quantum Transport

(Two-dimensional electron gases)

Experiment M2

(Room MB 009)



Advances physics lab course for Master students

RWTH Aachen

Contents

Introduction	1
1 Scattering in two dimensional electron gases	3
1.1 Phonon scattering	4
1.2 Defect scattering	5
1.3 Alloy scattering	5
1.4 Electron scattering	6
1.5 Transport and quantum relaxation time	6
2 Quantum transport phenomena	7
2.1 Basic description of 2DEGs in magnetic fields	7
2.1.1 The 2DEG's density of states	8
2.1.2 2DEG in a magnetic field	10
2.1.3 Zeeman effect	11
2.2 Shubnikov-de Haas oscillations	12
2.3 Quantum Hall effect	18
2.3.1 Classical Hall effect	18
2.3.2 Transition to the QHE	19
2.3.3 The localization picture	19
2.3.4 The edge channel picture	21
2.4 Comments on temperature and B field	25
2.4.1 Thermal activation of SdH minima	25
2.4.2 Systematic errors of the hall resistance	26
3 The Setup	29
3.1 Sample	29
3.2 Cryostat	30
3.3 Software	30
4 Experiment and analysis	33
4.1 Cooling down the cryostat	33
4.2 Tasks	34
Appendices	37

Lock-in amplifier	I
How to analyze the Shoubnikov-de Haas oscillations	V
Bibliography	VII

Assumed knowledge:

- ◊ Basic quantum mechanics
- ◊ Basic solid state physics

Suggested literature:

1. Ibach, H. und Lüth, H., *Festkörperphysik* (Springer Verlag)
2. Ashcroft, N. W. und Mermin, N. D., *Solid State Physics* (International Edition, W. B. Saunders Company)
3. Datta, S., *Electronic Transport in Mesoscopic Systems* (Cambridge University Press)
4. Ferry, D. K., *Semiconductors* (Macmillan Publishing Company)
5. Ihn, T., *Semiconductor Nanostructures* (Oxford University Press)

Introduction

Due to the ongoing miniaturization of electronic components, especially in case of the transistor, quantum mechanical effects gain influence on electron transport in reduced dimensions. Without a profound knowledge of the relevant physics in this field, it is impossible to derive new functional structures and understand the observed transport phenomena. A prime example displaying the fundamental changes to transport characteristics in semiconductors in the quantum regime is the quantum Hall effect. Klaus von Klitzing received the Nobel prize for its discovery in 1985. The peculiar changes to the density of states of a two dimensional electron gas under the influence of an external magnetic field will be discussed in detail. It is the goal of this experiment to gain first experiences in low-dimensional transport measurements in semiconductors by thoroughly investigating the quantum Hall effect and related phenomena. Additionally, the extraction of material specific quantities from the transport data will be trained.

Chapter 1

Scattering in two dimensional electron gases

In this chapter we review a few basic transport related quantities and their microscopic origins. A central approach to describe electrons in solids is based on Bloch waves. In this single particle picture, a perfectly periodic lattice potential does not lead to scattering of the electrons. Perturbations of the periodicity are the only source of scattering, thus leading to a finite resistance in transport measurements.

Within the Drude model, all free electrons carry the electric current and the mean scattering time τ is introduced to account for the time between two scattering events. τ is also the characteristic relaxation time, which the electronic system needs to return to its thermal equilibrium from any perturbation. However, due to the Pauli principle, electrons away from the Fermi surface are not able to gain energy from an electric field, because all energetically reachable states are occupied. Proportional to τ and also a measure for how sensitive electrons react to an applied electric field is the mobility

$$\mu = \frac{e}{m^*} \tau_{\text{tr}}(E_F), \quad (1.1)$$

with e being the elementary charge and m^* the effective mass. Throughout this instruction, the charge of an electron will be $q = -e$. We now also specify τ_{tr} as being the relaxation time probed by transport, thus only the electrons at the Fermi Energy contribute. Adding the charge carrier concentration n_s and the length l and width w of the probed sample area, we are able to calculate the sample resistance R_{xx} **excluding** an external magnetic field via

$$R_{xx} = \frac{l}{w} \cdot \frac{1}{\sigma_{xx}} = \frac{l}{w} \cdot \frac{1}{n_s e \mu}. \quad (1.2)$$

σ_{xx} is the x-component of the conductivity tensor and since we are treating two dimensional systems, the thickness does not appear in the above equation and the dimension of $n_s = \text{m}^{-2}$.

Multiple sources of scattering are found in semiconductors. The resulting individual contributions τ_i to the mean transport scattering time may be summed in case of independent scattering mechanisms.

$$\frac{1}{\tau_{\text{tr}}} = \sum_i \frac{1}{\tau_i} \quad (1.3)$$

The different contributions do not only vary in strength but also significantly in their temperature dependencies, which will now be discussed in further detail.

1.1 Phonon scattering

A phonon is a quantum mechanical quasi particle, which posses energy $\hbar\omega$ and momentum $\hbar k$. Phonons represent the vibrational motion of collectively excited lattice atoms, oscillating around their equilibrium positions. The quasi particles are delocalized, meaning no specific location may be attributed to them. Increased temperature leads to greater dislocation from the equilibrium positions, thus disturbing the lattice periodicity and causing scattering of the electrons.

One distinguishes between optical and acoustic phonons. The latter may be thought of as sound waves, propagating through the crystal. In this case the atoms within a unit cell always move in phase. This is not true for optical phonons, where the atoms oscillate out of phase. In case of differently charged sublattices, the vibration induces oscillating dipole moments (fig. 1.1), which interact with photons. Therefore these modes are called 'optical'.

As a rule of thumb, the electronic transport in 2DEGs is limited by optical phonon scattering above 60 K. Acoustic phonons limit binary semiconductors between 10 K and 50 K and ternary between 40 K and 50 K. Below 10 K phonon scattering becomes negligible. The temperature dependence of the scattering rate of the acoustic phonons may be derived

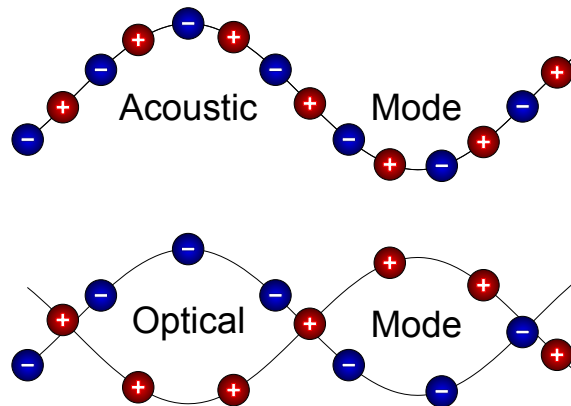


Figure 1.1: Comparison of transverse acoustic and optical phonons with the same wave length for a material with a two atom basis.

by a few plausible arguments. The number of scattering events in a certain time interval is proportional to the scattering cross section Σ and the thermal average over all electron velocities $\langle v \rangle$, meaning $\tau \sim (\Sigma \cdot \langle v \rangle)^{-1}$. For sufficiently high temperatures, the electronic transport through the heterostructure is not yet confined to the area of the 2DEG and

$\langle v \rangle$ is proportional to \sqrt{T} as for a three dimensional semiconductor. Since the scattering cross section may be considered proportional to the square of the oscillation amplitude of a phonon, which is proportional to T , the result is:

$$\tau_{ph} \sim T^{-\frac{3}{2}} \quad (1.4)$$

With lower temperature, the probability to excite a phonon is reduced, thereby increasing the mean time between two scattering events.

1.2 Defect scattering

Any disturbance of the periodicity of the lattice potential, either unintentional due to impurities and vacancies or intentional due to dopants, leads to scattering. Usually, this effect dominates below 10 K.

In analogy to phonon scattering, the temperature dependence of the relaxation time τ_{ds} depends on the scattering cross section Σ_{ds} . Since the interaction of an electron with a charged defect is described by *Rutherford scattering*, Σ_{ds} is inversely proportional to the fourth power of the particles' velocity. Thus τ_{ds} will be proportional to $\langle v \rangle^3$ in the end. For sufficiently low temperatures transport is limited to the 2DEG and the electron velocity does not depend on temperature. It follows:

$$\tau_{ds} \sim T^0 \quad (1.5)$$

Compared to conventional semiconductors, a 2DEG behaves like a metal at low temperatures.

1.3 Alloy scattering

Alloy scattering occurs in different III-V semiconductors like $\text{Al}_x\text{Ga}_{1-x}\text{As}$ or $\text{In}_x\text{Ga}_{1-x}\text{As}$. The statistical occupation of valence-III lattice sites by either Gallium and Aluminum or Gallium and Indium introduces a weak arbitrary potential, which leads to scattering of the electrons. In AlGaAs/GaAs heterostructures electrons are mainly confined to the GaAs, therefore alloy scattering is reduced. However, in InGaAs/InP heterostructures the 2DEG lives in the alloy and is dominated by alloy scattering for low temperatures ($T \leq 40$ K). Like defect scattering, alloy scattering is temperature independent for low temperatures.

1.4 Electron scattering

Due to the conservation of the total momentum of the electrons, electron-electron scattering does not play a role for the calculation of the transport relaxation time. The mobility of the 2DEG is mainly governed by the scattering with phonons, defect scattering and alloy scattering.

1.5 Transport and quantum relaxation time

As previously discussed, one may extract the transport relaxation time from measurements of the sample resistance. However, this quantity is not suitable to calculate the components of equation 1.3. This is due to the requirement, that for an electron to contribute to a measurable resistance, it needs to reduce its momentum component parallel to the outer electric field significantly. If $S(\Theta)$ represents the probability to be scattered at an angle Θ from the direction of transport, then the transport relaxation time is:

$$\frac{1}{\tau_{\text{tr}}} = \int_0^\pi d\Theta S(\Theta)(1 - \cos \Theta) \quad (1.6)$$

The term $(1 - \cos \Theta)$ accounts for the relative weight according to the above argument. The quantum relaxation time τ_q , which is the life time of an electron in a certain single particle state, describes the mean time between two scattering events. In this case it does not play a role how big the deflection from the direction of transport is, thus

$$\frac{1}{\tau_q} = \int_0^\pi d\Theta S(\Theta). \quad (1.7)$$

Thereby, within the boundaries of the discussed scattering mechanisms, $\tau_{\text{tr}} \geq \tau_q$.

Chapter 2

Quantum transport phenomena

2.1 Basic description of 2DEGs in magnetic fields

In order to create semiconductor heterostructures, epitaxial growth methods are utilized. Combining suitable materials and paying close attention to the thickness of the different layers is essential. Materials with similar but different band gaps and lattice constants are grown in a layer-by-layer fashion, leading to the formation of a two dimensional electron gas, if done correctly (fig. 2.1). In our example, a combination of barely doped InGaAs and

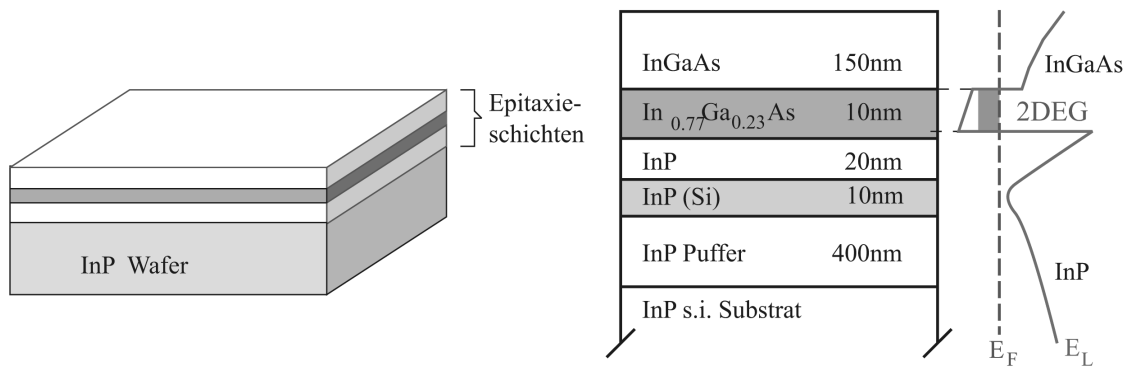


Figure 2.1: Layers of an InGaAs/InP heterostructure and schematic development of the conduction band energy relative to the Fermi energy.

highly n-doped InP is used. InP shows a much larger band gap than InGaAs. Growing them on top of each other lead to a bending of the conduction and valence bands at the boundary. However, the Fermi energy E_F remains constant across any material interface, while the sample is in equilibrium. In combination with the remaining discontinuities in the valence and conduction band ΔE_V and ΔE_L , a bending of the conduction band towards E_F inside the InGaAs results. Due to the large band gap mismatch, the conduction band is pushed beneath E_F at the InGaAs/InP interface. Hence a triangular potential well develops beneath E_F (fig. 2.2), hosting electrons in a very narrow layer, extending perpendicular to the direction of growth. Due to the strong confinement, it is called a

two-dimensional electron gas.

The electrons move freely in the 2DEG, only limited by the different sources of scattering. In order to reduce electron scattering originating from the donor atoms in the InP layer, an additional thin spacer layer (typically 10 – 40 nm) of undoped InP is added to the stack. Increasing the distance to the ionized donor atoms in the n-InP layer increases the mobility greatly (fig. 2.1).

The strong confinement of the electrons within the triangular potential well leads to

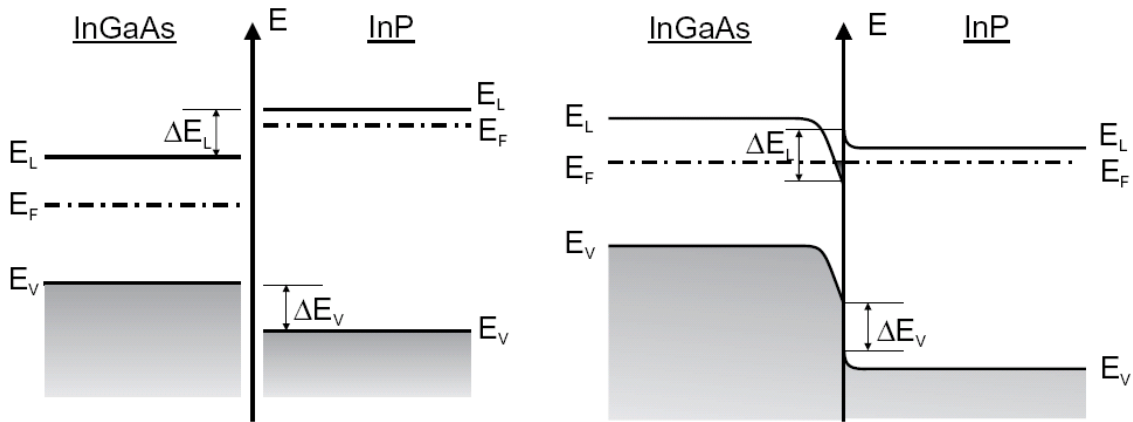


Figure 2.2: Schematic depiction of bands at an InGaAs/InP interface. E_L : Conduction band edge, E_V : Valence band edge, ΔE_L : Conduction band discontinuity, ΔE_V : Valence band discontinuity. (left) Not in contact. (right) In contact.

a quantization of electronic states in the z-direction of growth. Freely moving electrons portray a parabolic energy dispersion, which remains valid for the kinetic energy in the xy-plane. However, in z-direction subbands E_z^j form, which basically offset identical parabolae. Thus the total kinetic energy is described by:

$$E^j(k_x, k_y) = \frac{p_x^2 + p_y^2}{2m^*} + E_z^j = \frac{\hbar^2 k_x^2 + \hbar^2 k_y^2}{2m^*} + E_z^j, \quad j = 0, 1, 2, \dots \quad (2.1)$$

Here m^* is the effective mass of the electrons, which is determined by the curvature of the band structure. $k = \frac{2\pi}{\lambda} = \frac{p}{\hbar}$ is the electron's wave vector.

In the vast majority of samples, the degree of doping is adjusted to only fill states in the $j = 0$ subband. At low temperatures and thus very limited thermal excitation, all electrons occupy states belonging to E_z^0 . Therefore, the extension of the electrons' wave function in z-direction will correspond to the E_z^0 state. Since this extension will be finite, one also refers to quasi-2DEGs.

2.1.1 The 2DEG's density of states

For the following argumentation, the finding below is paramount:

The density of states (DOS), meaning the number of states which may be occupied in a certain energy interval, is constant in a two dimensional system [1].

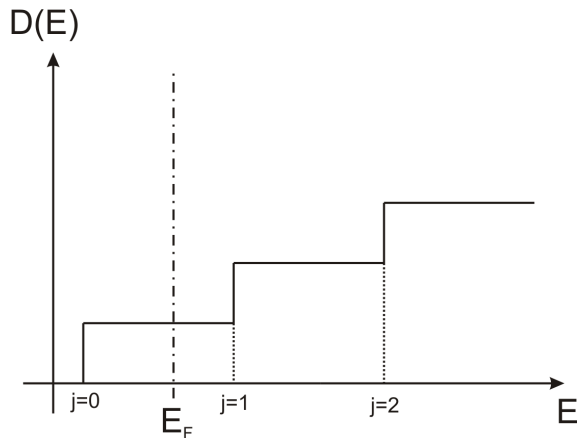


Figure 2.3: Density of states of a 2DEG without magnetic field. A stepwise increase for the onset of the different subbands $j = 0, 1, 2$ is visible.

We will now take a closer look at the deduction. In a 2D system of dimensions L_1 and L_2 , the electrons may possess the wave numbers $k_i = n \frac{2\pi}{L_i}$ and every state in the 2D k-space (k_x, k_y) is attributed with an area of $\frac{4\pi^2}{L_1 L_2}$. All states with energy $E = \frac{\hbar^2 \vec{k}^2}{2m^*}$ lie on a circle with radius $k = |\vec{k}|$ in k-space. Thus the total number of states belonging to a certain energy is

$$Z = \frac{\pi k^2}{\frac{4\pi^2}{L_1 L_2}} = \frac{L_1 L_2}{4\pi} \cdot \frac{2m^* E}{\hbar^2} \cdot g_s g_v. \quad (2.2)$$

The spin degeneracy factor $g_s = 2$ is a manifestation of Pauli's principle, describing the possibility to occupy every state with two electrons of opposite spin $s = \pm \frac{1}{2}$. The valley degeneracy factor is $g_v = 1$ for InGaAs/InP and is higher for other systems like silicon ($g_v = 6$), germanium ($g_v = 8$) or graphene ($g_v = 2$)[2, p. 38-39]. It describes the possibility to find multiple equivalent constant energy surfaces in the first Brillouin zone, which follow the same dispersion relation. The dispersion relations' origins only lie at different k-points, usually high symmetry points like X, L or K. Valley degeneracy is only lifted in high magnetic fields.

In our case, we only care about the number of electrons which are allowed to occupy a certain area $Z_s = \frac{Z}{L_1 L_2}$. From its derivative $\frac{dZ_s}{dE}$, we gain the information on how many states are available around a certain energy. Thus, the density of states (DOS) $D^j(E)$ at energy E in subband j is given by:

$$D^j(E) = \frac{dZ_s}{dE} = g_s g_v \cdot \frac{m^*}{2\pi \hbar^2} = \text{const.} \quad (2.3)$$

If the number of electrons is large enough to start filling an additional subband, a jump occurs in the density of states (compare fig. 2.3). Since we assume to only occupy the first subband, we will use a constant DOS $D(E)$ for all considered energies. Thus, the charge carrier density per unit area n_s reads

$$n_s = \int_0^{E_F} D(E)dE = g_s g_v \cdot \frac{m^*}{2\pi\hbar^2} \cdot E_F. \quad (2.4)$$

2.1.2 2DEG in a magnetic field

Applying a magnetic field of strength B perpendicular to the 2DEG constrains the motion of the electrons even further. Classically, electrons are forced on cyclotron orbits with frequency $\omega_c = \frac{eB}{m^*}$. In a quantum mechanical picture, electrons now occupy states belonging to quantized energy eigenvalues with distance $\hbar\omega_c$, called Landau levels (LLs). We find the total energy of the electrons

$$E_n^j = E_z^j + \hbar\omega_c(n + \frac{1}{2}) + s\mu_B g B, \quad n = 0, 1, 2, \dots \quad (2.5)$$

Here n is a new quantum number called the LL index. The last term treats the two possible spin projections in the magnetic field, with $s = \pm \frac{1}{2}$ being the spin quantum number, μ_B the Bohr magneton $\frac{e\hbar}{2m_e}$ and g the Landé factor. Therefore, the 2D-DOS (eq. 2.3) splits up in a sequence of δ -peaks at finite magnetic fields. This is schematically shown in figure 2.4. The broadening of the LLs originates from potential fluctuations in the sample, which are due to any defect or ionized atom within or adjacent to the layer supporting the 2DEG. An electron moving on a specific cyclotron orbit, thus belonging to a certain LL, may do so in a potential valley or on top of a potential hill. Thereby, the sharp energy of a LL is smeared out by the degree of potential roughness.

The splitting of LLs due to the spin degree of freedom, following equation 2.5, is not included at this point, since $m^* \ll m_0$ (m_0 being the free electron's mass) is small compared to $\hbar\omega_c$.

As the condensation of states into LLs happens homogeneously, meaning it will be comprised of states $E_n^j \pm \frac{1}{2}\hbar\omega_c$, it is straight forward to calculate the number of states in every LL, also called its degeneracy.

$$\text{Degeneracy of a LL: } N_L = D^j(E)\hbar\omega_c = \frac{eB}{h} \cdot g_s g_v = \frac{B}{\phi_0} \cdot g_s g_v. \quad (2.6)$$

$\phi_0 = h/e$ is the fundamental quantum of flux. The last expression fosters the picture, that for every flux quantum there is one state available in each LL. Classically speaking, the electrons perform their cyclotron motion centered around a flux quantum. The quantum number, which distinguishes between the different states is the location on the sample. If

one assumes, that the flux quanta are distributed homogeneously over the sample, then this ensues a homogeneous charge carrier distribution for a completely filled LL. For an arbitrary number of charge carriers, a certain number of LLs will be filled.

$$\text{Number of filled (degenerate) LLs: } \frac{n_s}{N_L} = \frac{hn_s}{eB} \cdot \frac{1}{g_s g_v} \quad (2.7)$$

Only reaching high magnetic fields will lift the spin and valley degeneracies. However, the

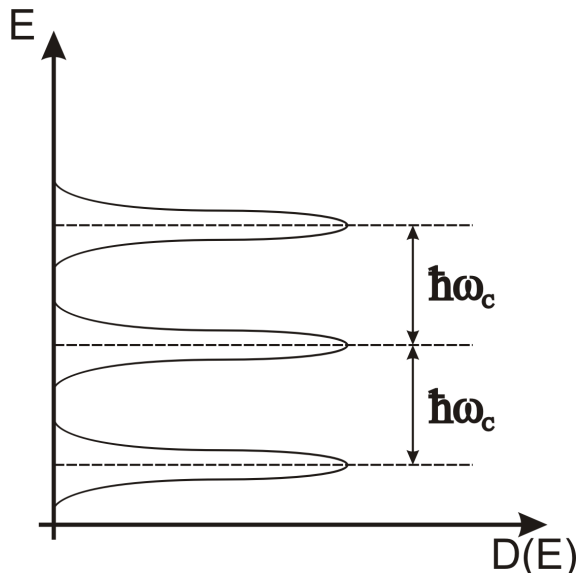


Figure 2.4: Condensation of states into Landau levels with the energetic difference $\hbar\omega_c$.

very frequently used filling factor ν describes the number of filled LLs, which are neither spin nor valley degenerate.

$$\nu = \frac{hn_s}{eB} \quad (2.8)$$

In the InGaAs/InP system under investigation, each filled LL will contribute a filling factor of $\nu = 2$, as long as the spin degeneracy is not lifted. For other materials like silicon ($g_v = 6$), filling one fully degenerate LL will add a filling factor of $\nu = 12$.

2.1.3 Zeeman effect

We will now treat the electron spin in more detail. The description arises from the magnetic dipole moment μ , which will orient itself relative to a magnetic field. This additional degree of freedom is quantum mechanically defined by a spin operator

$$\mathbf{S} = \frac{1}{2}\boldsymbol{\sigma}, \quad (2.9)$$

where the components of σ are Pauli matrices:

$$\boldsymbol{\sigma}_x = \begin{pmatrix} 0 & 1 \\ 1 & 0 \end{pmatrix}, \boldsymbol{\sigma}_y = \begin{pmatrix} 0 & -i \\ i & 0 \end{pmatrix}, \boldsymbol{\sigma}_z = \begin{pmatrix} 1 & 0 \\ 0 & -1 \end{pmatrix}$$

The magnetic moment of the electron is given by

$$\boldsymbol{\mu} = -\frac{1}{2}g\mu_B\boldsymbol{\sigma}, \quad (2.10)$$

with $\mu_B = e\hbar/2m_e$ the Bohr magneton and $g = 2.0023$ the Landé factor. μ_B has a value of $9.274 \cdot 10^{-24} \text{ Am}^2 = 57.88 \text{ } \mu\text{eV/T}$.

In an external magnetic field of strength B , the magnetic moment feels a turning moment of

$$\boldsymbol{M} = \boldsymbol{\mu} \times \boldsymbol{B}. \quad (2.11)$$

The corresponding Schrödinger equation is the Pauli equation:

$$i\hbar \frac{\partial}{\partial t} | s \rangle = -\frac{1}{2}g\mu_B\boldsymbol{\sigma}\boldsymbol{B} | s \rangle \quad (2.12)$$

Here $| s \rangle$ is a general spin state, comprised of a superposition of $|\uparrow\rangle$ and $|\downarrow\rangle$. $|\uparrow\rangle$ and $|\downarrow\rangle$ represent the parallel and anti parallel orientation of the spin regarding the magnetic field. Assuming a magnetic field in z-direction, the Pauli equation reads

$$i\hbar \frac{\partial}{\partial t} | s \rangle = -\frac{1}{2}g\mu_B\sigma_z B_z | s \rangle, \quad (2.13)$$

yielding the energy eigenvalues

$$E_{\pm} = \mp \frac{1}{2}g\mu_B B_z \quad (2.14)$$

Thus, the external magnetic field lifts the spin degeneracy and the energy splitting

$$\Delta E = E_+ - E_- = g\mu_B B \quad (2.15)$$

is called Zeeman energy. Importantly, it is linear in B . In the QHE context, the Zeeman effect manifest as a splitting of LLs. For high magnetic fields it is clearly visible. In the small field limit however, inherent broadening of the LLs undermines a sufficient separation and thermal broadening also disguises the observation.

2.2 Shubnikov-de Haas oscillations

We will now describe the actual transport measurement and explain its characteristic features. Using a Hall bar sample geometry as in figure 2.5, one is able to comfortably extract

the longitudinal (parallel to the direction of current) and transverse (perpendicular to the direction of current) resistance. We will refer to them as R_{xx} and R_{xy} respectively. These two quantities permit a detailed analysis of the specific features of a semiconductor.

Actually, the Hall bar is designed to carry out an ideal four probe measurement. Most importantly, the voltage probes are separated from the source and drain electrodes, which provide the current. If the voltages are probed by a highly resistive measurement device (10 MΩ input resistance of the lock-in), no significant current will pass through the contacts, which always have a finite resistance. Thus there will be no voltage drop across them ($U = R \cdot I$, $I = 0$) and one will accurately measure the chemical potentials in the 2DEG induced by the source-drain current. The mathematical description of the transport

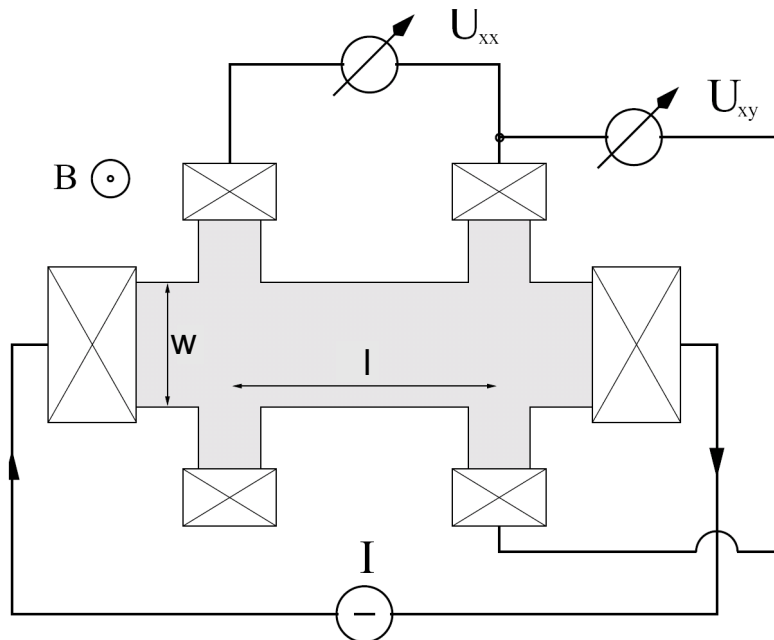


Figure 2.5: Schematic depiction of a four probe measurement of the longitudinal and transverse resistance. The sample is equipped with a source and drain contact, as well as four voltage probes.

through the 2DEG is centered around the conductivity matrix

$$\vec{\sigma} = \begin{pmatrix} \sigma_{xx} & \sigma_{xy} \\ -\sigma_{xy} & \sigma_{xx} \end{pmatrix} \text{ and } \vec{j} = \vec{\sigma} \cdot \vec{E} \implies \vec{\sigma} \begin{pmatrix} U_{xx} \\ U_{xy} \end{pmatrix} = \begin{pmatrix} I_x \\ I_y \end{pmatrix} \quad (2.16)$$

Here \vec{j} is the current density, which is defined as $j_x = I_x/w$ in our 2D case, where w is the width of the sample. Additionally, we need the resistivity matrix, which follows from matrix inversion $\vec{\rho} = \vec{\sigma}^{-1}$.

$$\vec{\rho} = \begin{pmatrix} \rho_{xx} & \rho_{xy} \\ -\rho_{xy} & \rho_{xx} \end{pmatrix} \text{ and } \vec{E} = \vec{\rho} \cdot \vec{j} \implies \begin{pmatrix} U_{xx} \\ U_{xy} \end{pmatrix} = \vec{\rho} \begin{pmatrix} I_x \\ I_y \end{pmatrix} \quad (2.17)$$

We will first focus on R_{xx} . A LL, which energetically resides beneath the Fermi energy, is filled with N_L electrons at sufficiently low temperatures. Increasing the magnetic field entails two effects. On the one hand, the energetic separation $\hbar\omega_c$ of two LLs increases linearly with B . On the other, the degeneracy of a LL N_L also increases linearly with B (eq. 2.6). This leads to a redistribution of electrons among the LLs to always occupy the energetically most favorable states. For the following discussion we will assume $T = 0$, so that the Fermi energy is positioned at the energetically highest occupied state, and a constant charge carrier concentration.

As shown in figure 2.6, coming from $B = 0$ T, the DOS transforms from a constant to a

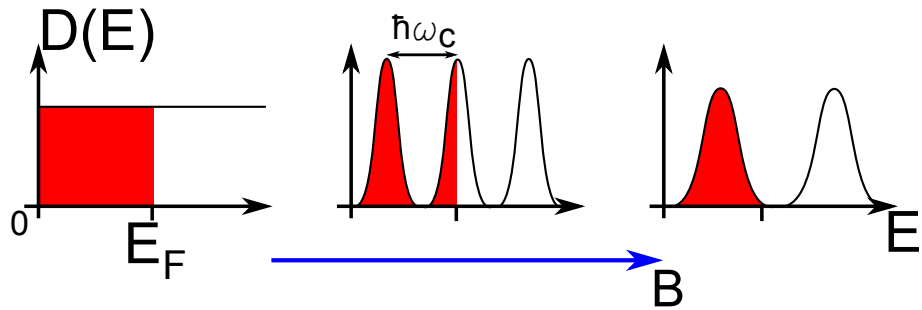


Figure 2.6: Development of the DOS of a 2DEG in an increasing magnetic field from left to right.

densely packed Landau level spectrum. Further increasing B will subsequently push the LLs over E_F , as the energetic distance and degeneracy of the LLs simultaneously increase. Since the charge carrier density is constant, the number of filled states below E_F is also constant. Therefore as B increases, E_F will quickly move from an almost empty LL to the next filled LL, because the DOS on the edges of the LLs is very small compared to the center. If one now looks at the position of E_F dependent on the external magnetic field (fig. 2.7), it will first follow a straight line, while the energy of the last partially filled LL increases. Once this LL is empty, E_F jumps to the highest occupied state of the next underlying LL and will move upwards again, until that LL is also depleted. The idealized behavior of figure 2.7 is only valid for delta shaped LLs. In real samples, the previously discussed broadening smears out the strongly varying DOS at E_F , as the LLs cross E_F . More involved calculations show that this variation entails a strongly varying relaxation time τ_{tr} . In the tails of a LL, screening of the disorder potential is limited. Therefore scattering is enhanced and mobility is reduced. Actually, the bulk of the sample may even disaggregate and form a network of interconnected quantum dots. For further reading on this topic see references [3, 4].

As a rule of thumb we are able to conclude:

$$\text{small DOS } D(E_F) \longrightarrow \text{small mobility } \mu$$

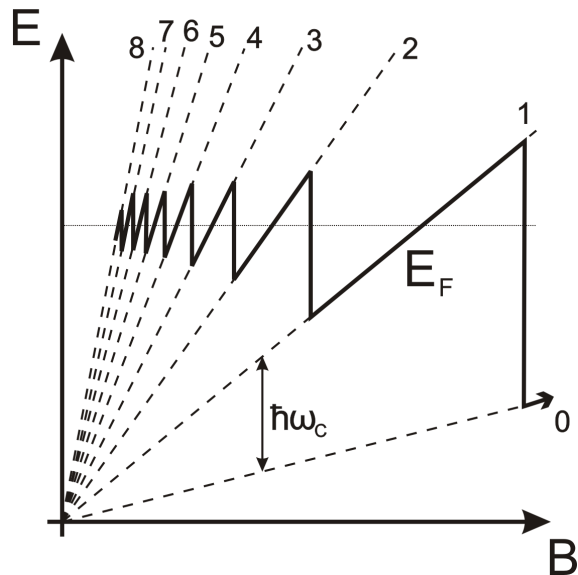


Figure 2.7: Idealized position of the Fermi energy as the magnetic field is swept and different LLs are populated. [5].

Therefore, whenever a LL is full and E_F sits between two LLs, one finds a minimum in the conductivity σ_{xx} . The crux of dealing with a conductivity matrix lies in its inverse, the resistivity matrix. The longitudinal element reads

$$\rho_{xx} = \frac{\sigma_{xx}}{\sigma_{xx}^2 + \sigma_{xy}^2}. \quad (2.18)$$

Surprisingly, one also finds a minimum for the resistivity.

σ_{xx} and ρ_{xx} simultaneously acquire minimal values.

Obviously, the resistance R_{xx} will oscillate as B is swept, giving rise to the designation Shubnikov-de Haas oscillations (fig. 2.8). Using equation 2.6 yields an expression for the distance of these oscillations. For the i th minimum it reads:

$$n_s = i \cdot N_L = i \cdot g_s g_v \cdot \frac{eB_{(i)}}{h} \Rightarrow \frac{1}{B_{(i)}} = \frac{i g_s g_v e}{h n_s} \quad (2.19)$$

The same is true for the $(i+1)$ st minimum:

$$n_s = (i+1) \cdot N_L = (i+1) \cdot g_s g_v \cdot \frac{eB_{(i+1)}}{h} \Rightarrow \frac{1}{B_{(i+1)}} = \frac{(i+1) g_s g_v e}{h n_s} \quad (2.20)$$

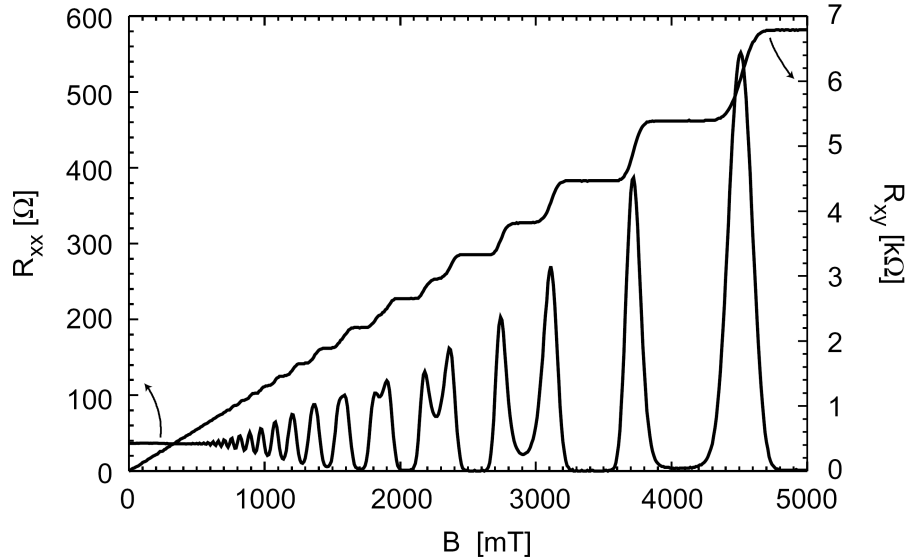


Figure 2.8: Longitudinal resistance R_{xx} and transverse resistance R_{xy} of a 2DEG. Shubnikov-de Haas Oscillations and Hall-plateaus are very pronounced.

Therefore, two consecutive minima obey the expression:

$$\Delta\left(\frac{1}{B}\right) = \frac{1}{B_{(i+1)}} - \frac{1}{B_{(i)}} = g_s g_v \cdot \frac{e}{h n_s} \quad (2.21)$$

In essence, the Shubnikov-de Haas minima are periodic in $\frac{1}{B}$. Using 2.21, one is also able to make a statement about the charge carrier concentration n_s :

$$n_s = g_s g_v \cdot \frac{e}{h} \left(\frac{1}{B_{(i+1)}} - \frac{1}{B_i} \right)^{-1} \quad (2.22)$$

A detailed calculation of the longitudinal sample resistance R_{xx} , for moderate magnetic fields, under consideration of the Fermi distribution for finite temperatures and a finite lifetime of the electronic states yields:

$$\frac{R_{xx}(B)}{R_{xx}(B=0)} \approx 1 + 2 \cdot \underbrace{\cos\left(2\pi\left(\frac{E_F}{\hbar\omega_c} - \frac{1}{2}\right)\right)}_a \cdot \underbrace{\exp\left(-\frac{\pi m^*}{\tau_q e B}\right)}_b \cdot \underbrace{\frac{X}{\sinh X}}_c \cdot \underbrace{\cos\left(2\pi\left(\frac{g\mu_B B}{2\hbar\omega_c}\right)\right)}_d \quad (2.23)$$

where

$$X := \frac{2\pi^2 k_B T}{\hbar\omega_c}$$

The components a to d have the following meanings.

- a) The first term is the analytic representation of the above discussed oscillations in

R_{xx} with B . The cosine implements the $\frac{1}{B}$ periodicity of the Shubnikov-de Haas oscillations.

- b) The finite lifetime of the conduction band electrons in the 2DEG, due to scattering (see section 2.1.2), leads to a partial lifting of the LL degeneracy. This results in a Lorenzian broadening of the LLs with a full width at half maximum Γ . Like in the case of thermal broadening, the amplitude of the oscillations in R_{xx} is damped, depending on the ratio of $\Gamma = \frac{\hbar}{2\tau_q}$ and $\hbar\omega_c$.
- c) This term takes the thermal broadening of the Fermi distribution into account. The maxima in the resistance are lowered for higher temperatures, because the central parts of the LLs with high DOS will be slightly less populated, while E_F crosses the center. The damping depends on the relation of $k_B T$ and $\hbar\omega_c$, since a large separation of LLs at high B will suppress the excitation of electrons into higher LLs.
- d) Since high magnetic fields lead to a lifting of the spin degeneracy, this oscillating term incorporates the effect of the Zeeman splitting in equation 2.5.

2.3 Quantum Hall effect

In this section we will briefly review the classical hall effect and then move on to discuss the model of the Quantum Hall effect (QHE).

2.3.1 Classical Hall effect

The classical Hall effect describes the development of an electric force eE_H , normal to the direction of current. This force compensates the Lorentz force, which deflects charge carriers to one side of a conductive sample with perpendicularly applied magnetic field. In a 2D system the expression reads

$$E_{\text{Hall}} = \frac{U_H}{w} = \underbrace{\frac{-B}{n \cdot t \cdot e}}_{n_s} \cdot \frac{I_x}{w} = \frac{-BI_x}{n_s e w}. \quad (2.24)$$

Here n is the electron density in units of cm^{-3} , t the sample thickness, w the width of the sample, B is the value of the magnetic field in z-direction and U_H is the Hall voltage measured normal to the direction of current. The Hall coefficient R_H links the voltage build-up with the current and magnetic field in the form

$$U_H = R_H BI_x = -\frac{BI_x}{n_s \cdot e}. \quad (2.25)$$

Thus the bare Hall coefficient reads

$$R_H = \frac{R_{xy}}{B} = -\frac{1}{n_s \cdot e}. \quad (2.26)$$

At this point it is also easy to calculate the Hall resistance, as well as the longitudinal resistance with the help of equations 1.1 and 1.2

$$R_{xy} = \frac{U_H}{I_x} = -\frac{B}{n_s \cdot e}, \quad R_{xx} = \frac{l}{w} \cdot \frac{m^*}{e^2 n_s \tau_{\text{tr}}} [\text{up}\Omega]. \quad (2.27)$$

Importantly, in 2D R_{xy} is identical to the element ρ_{xy} of the resistivity matrix (eq. 2.17). A detailed deduction may be found in reference [6]. Expressions 2.27 describe the classical Hall effect well for small magnetic fields. R_{xx} remains constant, whereas R_{xy} is proportional to B .

2.3.2 Transition to the QHE

As shown in equation 2.6, the degeneracy of a LL is solely dependent on the magnetic field. Therefore, whenever $n_s = i \cdot \frac{eB}{h}$, $i = 1, 2, 3 \dots$ an integer number of LLs will be filled. Inserting this into equation 2.27 results in

$$R_{xy} = \frac{B}{e \cdot n_s} = \frac{B}{e} \cdot \frac{h}{ieB} = \frac{h}{ie^2}. \quad (2.28)$$

Surprisingly, for fully filled LLs, the hall resistance is always an integer fraction of the quantity $\frac{h}{e^2}$, which only contains natural constants. Especially there is no contribution from the sample geometry. In a real experiment one observes wide plateaus for high magnetic fields at values $R_{xy} = \rho_{xy} = \frac{h}{ie^2}$. The center of these plateaus mark complete filling of the corresponding integer number of LLs. Conversely, this also entails a minimum in the SdH oscillations, as shown in figure 2.8.

By precisely measuring the sample current I_x and Hall voltage U_{xy} , it is possible to measure a resistance, which is independent of the sample geometry and other external influences. Therefore, this is the method of choice to define the resistance standard today. $R_K = \rho_{xy}(i = 1) = 25812.8\Omega$ is also known as von Klitzing constant.

Comment: In our experiment the spin degeneracy is only lifted for high magnetic fields, thus the quantization initially follows a twofold pattern. Equation 2.28 is modified and reads:

$$R_{xy} = \frac{h}{2ie^2}, \quad i = 1, 2, 3, \dots \quad (2.29)$$

In order to explain the QHE we will introduce the localization as well as the edge channel picture. Both focus on different aspects, therefore we will treat them separately.

2.3.3 The localization picture

We have seen in section 2.1.2 that the broadening of the LLs is the result of potential fluctuations, which determine the electrons' paths. We now descry two different situations. Electrons in the center of a LL may diffuse over the whole sample. In the strong disorder limit, this means they move in between the hills and valleys of the potential. In the weak disorder limit, electrons outside the center of the LL have screened the potential by localizing themselves in potential valleys and thus the central electrons delocalize their wave function over the whole sample. If the LL is almost full, electrons may only locate themselves in the places where the maximum electron density is not yet reached. This is

true for the former potential hills. Once a LL is completely filled and there is a uniform distribution of electrons, the original disorder potential is restored. Which limit applies is dependent on the potential fluctuations and the LL degeneracy. The more states there are per LL, the better are the electrons able to screen the potential. Thus it is possible to move from strong to weak disorder for higher magnetic fields. It should now be clear why electronic states in the center of a LL are called **delocalized** and away from the center **localized** (fig. 2.9). Figure 2.10 portrays the different situations for the strong disorder

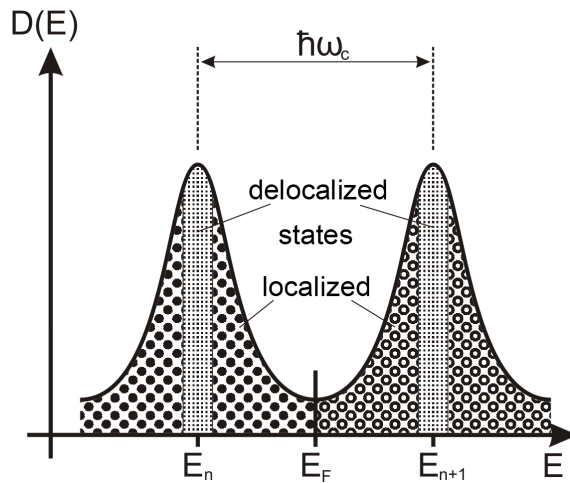


Figure 2.9: Landau levels composed of localized and delocalized states in the localization picture, after [7].

limit in a locally resolved scanning tunneling microscopy measurement. In the localization

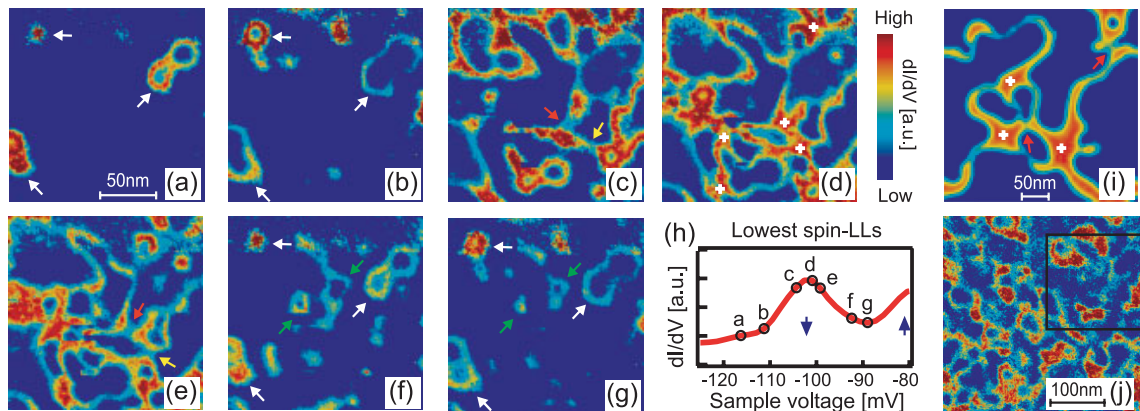


Figure 2.10: Depicted is the local density of states (LDOS) ($\propto dI/dV$) for the lowest Landau level at different energies at $B = 12$ T. In the sequence from a) to g) one sees the transition from localized states, which encircle potential valleys (white arrows), to delocalized states and back to localized states, which encircle potential hills (green arrows). For f) and g) the next LL already occupies the valleys again. From reference [8].

picture we are able to explain part of the QHE:

As the magnetic field is swept, the Fermi energy moves through the broadened LLs as

depicted in figure 2.9. As long as localized states are at the Fermi energy, there should be no contribution to conductivity and thus the sample should be highly resistive. Now, as long as σ_{xy} (thus ρ_{xy}) remains finite, tensor inversion yields $\rho_{xx} = 0$ (see section 2.2) and we measure $U_x = 0$. If the Fermi energy is in a region of delocalized states, conductivity will be finite and we can thereby explain the oscillating behavior of the longitudinal quantities. However, there is no reference to the impact of the actual sample geometry or contacts and there is no explanation for the quantization in the transverse direction.

2.3.4 The edge channel picture

We will now discuss the edge channel picture to explain the questions left behind by the localization picture.

In general, electrons occupy states in subbands beneath the Fermi energy [9]. Applying an external electrical field \vec{E} makes a redistribution of electrons towards states with a certain wave vector \vec{k} favorable. However, a few conditions need to be fulfilled.

1. Far below the Fermi energy all states are occupied, thus no redistribution is possible. Therefore only the region around the Fermi energy is of interest.
2. In order to find free states at the Fermi energy we need to demand a non-vanishing DOS there.

Additionally, the electric field will only lead to electrical conductivity, if the available states are not localized, thus we need to situate the Fermi energy at the center of the LLs. If we take the edge of the sample into consideration, we need to add a confining potential to our picture, since electrons can not leave the sample. Thus the energy of an electronic state is not only governed by its LL index according to $N_n = (n + \frac{1}{2})\hbar\omega_c$ and the disorder potential, but a strongly increasing edge potential is also added. Figure 2.11 (a) depicts the energies of multiple LLs across the sample, while neglecting the potential disorder. The effect of the edge potential is to lift the energy of the LLs towards the edge, forcing them to cross the Fermi energy at some finite distance from the edge. Now even if there are no states in the bulk of the sample, one will find lines of non-vanishing DOS where the LLs cross the Fermi energy along the edge. Since now our conditions for conductivity are fulfilled, we can constitute the formation of so called 1D **edge channels**. Classically the electrons at the edge of the sample can not perform their cyclotron motion without being scattered in a fashion that they move along the edge (fig. 2.11 (b)). Opposite edges will obviously counter propagate on paths called *skipping orbits*. Introducing defects on the paths of the electrons only leads to performing an additional full cyclotron orbit and subsequently resuming the original skipping orbit (fig. 2.11 (c)). Therefore inter-edge scattering is prohibited.

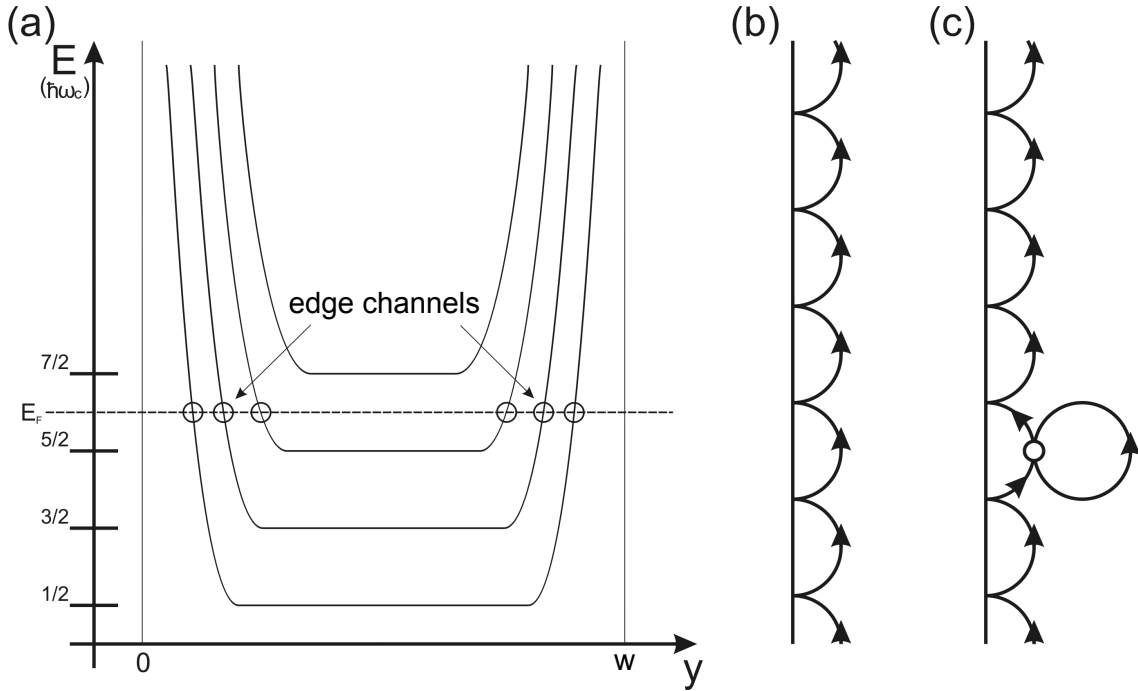


Figure 2.11: (a) Development of the LL energy across a sample with finite width (Neglecting potential disorder). (b) Skipping orbits along the edge of a sample and (c) their limiting impact on the occurrence of back scattering by defects. After [10].

In the edge channel picture, the conductance vanishes inside the sample, since only in the case of $E_F = (n + \frac{1}{2})\hbar\omega_c$ there will be free states for conduction.

Within the sample, the edge channel belonging to the lowest LL sits closest to the edge, because the corresponding electrons have the most energy to climb against the edge potential. If the Fermi energy crosses another LL, an additional edge channel is created. Since edge channels are one dimensional conductors, the current through them is

$$I = \frac{e}{h} \int_0^\infty f(E)dE = \frac{e}{h}\mu. \quad (2.30)$$

The quantity μ is called chemical potential and describes the energy at which the Fermi distribution $f(E) = \frac{1}{2}$. One may also view it as the average energy a particle needs to be added to the system. For vanishing temperature $\mu(T = 0) = E_F$. In equation 2.30 a contact with chemical potential μ_k , which may also be called reservoir, injects a current of $\frac{e}{h}\mu_k$ for every occupied edge channel. If we now calculate the current for every contact, we know that in a four point measurement no current flows via the voltage probes, thus $I_2 = I_3 = I_5 = I_6 = 0$. Contacts 1 (source) and 4 (drain) carry the entire current. Importantly, in equation 2.30 the chemical potential of the injecting contact enters. In order to find the net currents, we need to calculate the in- and outflowing currents for

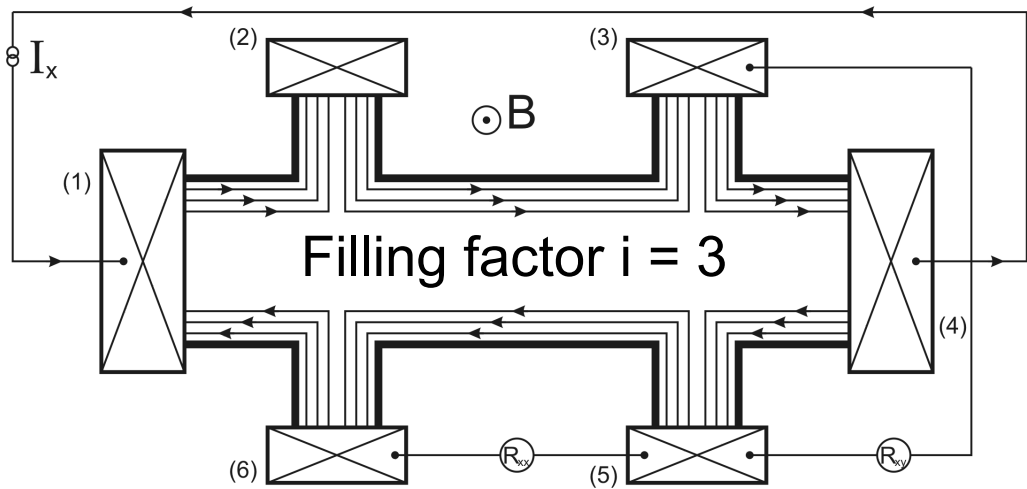


Figure 2.12: Depiction of a sample in Hall bar geometry. At filling factor $i = 3$, three counterpropagating edge channels run along opposite sides of the sample. Contacts (1) and (4) are used as source and drain for the current I_x , whereas contacts (2), (3), (5) and (6) are voltage probes for the transverse (R_{xy}) and longitudinal (R_{xx}) components. From [9].

every contact. The unidirectional and counterpropagating nature of the opposite edge channels simplifies the argumentation. If i is the number of filled edge channels we find the following table:

Overview of the contacts		
Contact	chem. potential	current
1	μ_1	$I = i \cdot \frac{e}{h}(\mu_1 - \mu_6)$
2	μ_2	$0 = i \cdot \frac{e}{h}(\mu_2 - \mu_1)$
3	μ_3	$0 = i \cdot \frac{e}{h}(\mu_3 - \mu_2)$
4	μ_4	$-I = i \cdot \frac{e}{h}(\mu_4 - \mu_3)$
5	μ_5	$0 = i \cdot \frac{e}{h}(\mu_5 - \mu_4)$
6	μ_6	$0 = i \cdot \frac{e}{h}(\mu_6 - \mu_5)$

The actually measured voltage difference ΔU between two contacts is directly proportional to their difference in chemical potential, since $\Delta\mu = e \cdot \Delta U$. This enables us to calculate the measurable resistances:

$$R_{xy} = \frac{U_H}{I} = \frac{(\mu_3 - \mu_5)/e}{I} \stackrel{(4,5)}{=} \frac{\mu_3 - \mu_5}{i(\mu_3 - \mu_5)e^2/h} = \frac{h}{ie^2} \quad (2.31)$$

$$R_{xx} = \frac{U_{xx}}{I} = \frac{(\mu_2 - \mu_3)/e}{I} \stackrel{(3)}{=} 0 \quad (2.32)$$

The Hall voltage is the result of the differing chemical potentials on either edge: $\Delta\mu = \mu_3 - \mu_5 \stackrel{(3,2,5)}{=} \mu_1 - \mu_4 = eU_{xy}$. This also means that in a constant voltage measurement

the Hall voltage becomes independent of the magnetic field in the QHE regime, as long as there is no back scattering between edge channels. It is also important to understand, that in this case the chemical potential on either side of the sample is constant. The change in the hall resistance mainly originates from the change in the number of conductive edge channels. In summary we find:

$$\text{Total current via } i \text{ edge channels} \quad I = i \cdot \frac{e}{h} \cdot eU_{xy}$$

$$\text{Hall resistance} \quad R_{xy} = \frac{h}{ie^2}$$

$$\text{conductivity per edge channel} \quad \delta\sigma = \frac{e^2}{h}$$

Hereby the quantization of the Hall resistance in the edge channel picture is explained. We conclude:

In the edge channel picture of the QHE, the Hall resistance displays quantized values $R_{xy} = \frac{h}{ie^2}$, while the longitudinal resistance vanishes. This behavior is caused by conductive stripes along the edge of the sample, one for each filled LL in the bulk of the sample. Every edge channel adds a conductance of $\sigma = \frac{e^2}{h}$.

Finally, we look at the strengths and weaknesses of the edge channel picture:

- ◊ Geometry and contacts of the sample are included.
- ◊ The Hall plateaus with values $\frac{h}{ie^2}$ follow from the 1D model.
- ◊ There is no insight concerning the transitions between the plateaus or their width.
- ◊ Prime assumption is the absence of back scattering, meaning counter propagating edge channels can not couple. If it fails, the calculation is vain.
- ◊ Localization is also needed, especially to justify the lack of back scattering.

2.4 Comments on temperature and B field

If we want to witness the Fermi energy crossing the LLs, we have to demand a small thermal broadening of the Fermi distribution $\Delta E \approx k_B \cdot T$ (k_B = Boltzmann's constant) compared to the energetic distance between neighboring LLs. Thus

$$\hbar\omega_c \gg k_B \cdot T \Rightarrow T \ll \frac{\hbar\omega_c}{k_B}, \quad (2.33)$$

leading us to the requirement of **low temperatures**. This is the main reason, besides the reduction of scattering, to use liquid helium as coolant. Additionally, we can further improve the above ratio by increasing ω_c , thus applying **high magnetic fields**. This means:

$$B \text{ large} \Rightarrow \mu B \gg 1 \Leftrightarrow \omega_c \tau \gg 1 \quad (2.34)$$

At high magnetic fields, electrons complete many cyclotron orbits before being scattered. This improves the visibility of the QHE. Many real measurements are therefore conducted below the temperature of liquid helium (4.2 K) and at magnetic fields above 10 T. Only in the high magnetic field regime one finds what is usually noted as the QHE: broad minima in R_{xx} with vanishing values, accompanied by broad and flat Hall plateaus in R_{xy} (compare fig. 2.8).

2.4.1 Thermal activation of SdH minima

If the Fermi energy is situated between two LLs, then the longitudinal resistance should ideally vanish. However, the energetic separation of the LLs might be too small, due to too low magnetic fields, or the temperature is too high and thus a significant number of delocalized states are populated. Coupling the edge channels will therefore lead to a finite resistance.

Obviously a higher temperature will provide more electrons with sufficient energy to jump from the Fermi edge to the next free delocalized state, thus increasing the resistance. Lower temperatures therefore entail lower resistance values in the SdH minima. This interplay is schematically illustrated in figure 2.13. Sure enough, the temperature dependence of the specific conductivity in a SdH minima follows an Arrhenius law [2, p. 308]

$$\sigma_{xx} = \sigma_0 \exp\left(-\frac{\Delta_{xx}}{2k_B T}\right), \quad (2.35)$$

with $\Delta_{xx}/2$ being the relevant activation energy and Δ_{xx} the distance between the two adjacent LLs. Only half of the energy is required, since an excitation from the Fermi energy to the next higher unoccupied extended state is sufficient to add to the resistance.

However, the equivalent process of depopulating the highest occupied extended state, by excitation to the Fermi energy and leaving a conductive hole behind, also needs to be taken into account.

Interestingly, in case of an odd filling factor, the activation energy corresponds to the Zeeman energy $g^*\mu_B B$ and thus allows us to extract the g-factor.

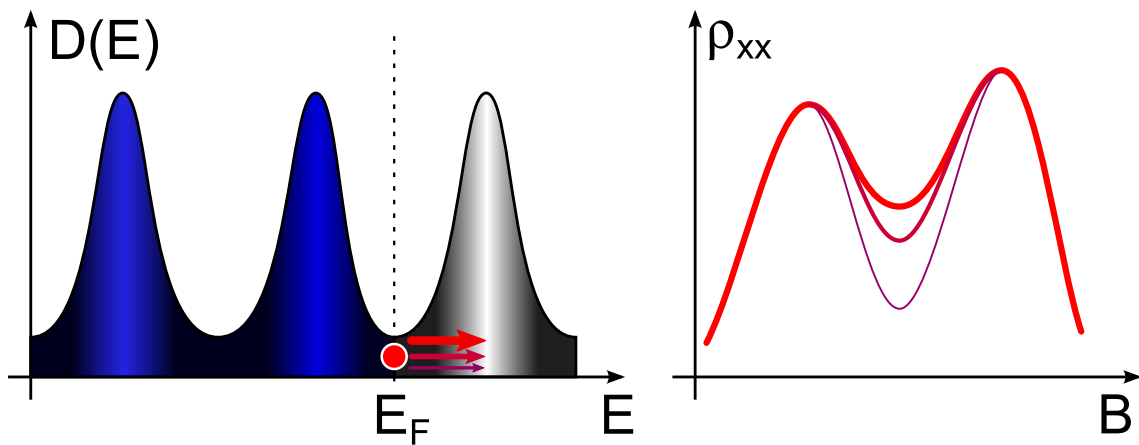


Figure 2.13: Depiction of the thermal activation of electrons sitting at the Fermi energy between two Landau levels. Previously localized electrons may occupy delocalized states in the center of the next empty LL and contribute to resistance. Higher temperatures enhance this mechanism and thereby decrease the visibility of minima in the conductivity.

2.4.2 Systematic errors of the hall resistance

Generally we have assumed, that solely the Hall voltage is picked up by two opposite contacts on the Hall bar. However, this is not possible to arbitrary precision, since fabrication imposes limits. Therefore, we have to account for an additional longitudinal voltage contribution (fig. 2.14). Fortunately, there is a way to get rid of this flaw. Measuring the

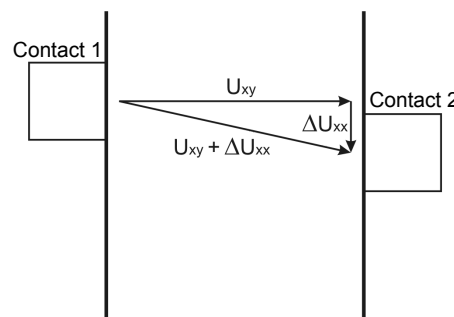


Figure 2.14: Schematic misalignment of two opposite contacts on a Hall bar. An additional longitudinal contribution ΔU_{xx} is picked up besides the Hall voltage U_{xy} .

Hall voltage for inverted magnetic field will change the sign of U_{xy} , but will leave U_{xx} un-

affected. In conclusion, we end up with values $U_{xy} + \Delta U_{xx}$ and $-U_{xy} + \Delta U_{xx}$. Obviously we find the pure Hall voltage by negating one value and subsequent averaging.

Chapter 3

The Setup

In our actual experimental configuration an InGaAs/InP heterostructure Hall bar sample has been installed inside a 4 K bath cryostat. It is contacted in four point geometry and allows the measurement of all elements of the resistivity tensor. The details of the applied lock-in technique are discussed in appendix 4.2.

3.1 Sample

The InGaAs/InP heterostructure Hall bar is shown in figure 3.1. The picture resolves a source and drain contact to the left and right, as well as three voltage probes on the top and bottom. Thereby we are able to inject a current and measure the longitudinal and transverse resistances independent of contact resistances.

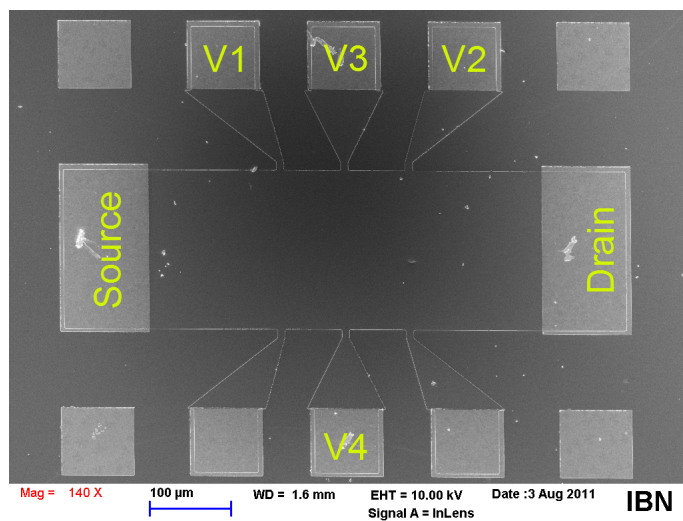


Figure 3.1: Scanning electron microscope picture of the sample and labeled contacts as used.

3.2 Cryostat

The setup is a custom build Helium bath cryostat. Figure 3.2 shows a schematic drawing of the components. The cryostat itself has an outer insulation vacuum, which protects the liquid Nitrogen (LN) shield from heat conductance to the outside. The shield itself is supposed to limit heat conductance and radiation impacting the liquid Helium (LHe). Latter is separated from the LN by an inner insulation vacuum, which is constantly pumped by a turbo pump. The sample sits in the center of the superconducting 6 T Titan-Niobium magnet, which has been fixed to an insert resting within the LHe. The helium bath may be monitored by pressure valves and is connected to an additional rotary pump. The pump is used to reduce the base temperature from 4.2 K down to roughly 2.2 K. Limiting the pumping speed with a valve makes it possible to stabilize the temperature at intermediate values.

Comment: The magnet may only be used in its superconducting state, since currents up to 50 A are used. If the magnet switches to the normal resistive state at high currents, a huge amount of energy is quickly dissipated, possibly damaging the magnet and the cryostat. Avoid quenching the magnet by all means! Therefore it is prohibited to change any limit values, like maximum voltage, manually on the magnet's current source. Additionally you will be required to keep track of the helium level inside the cryostat, by marking it on the outside.

3.3 Software

During the preparations and the cool down of the sample, all relevant values may be read from the lock-in and the temperature controller. The data of the SdH-oscillations and QHE are collected with a LabView program. Only the parameters for the magnetic field and the sweep rate are entered. The readings from the lock-in and magnet's current source are automated.

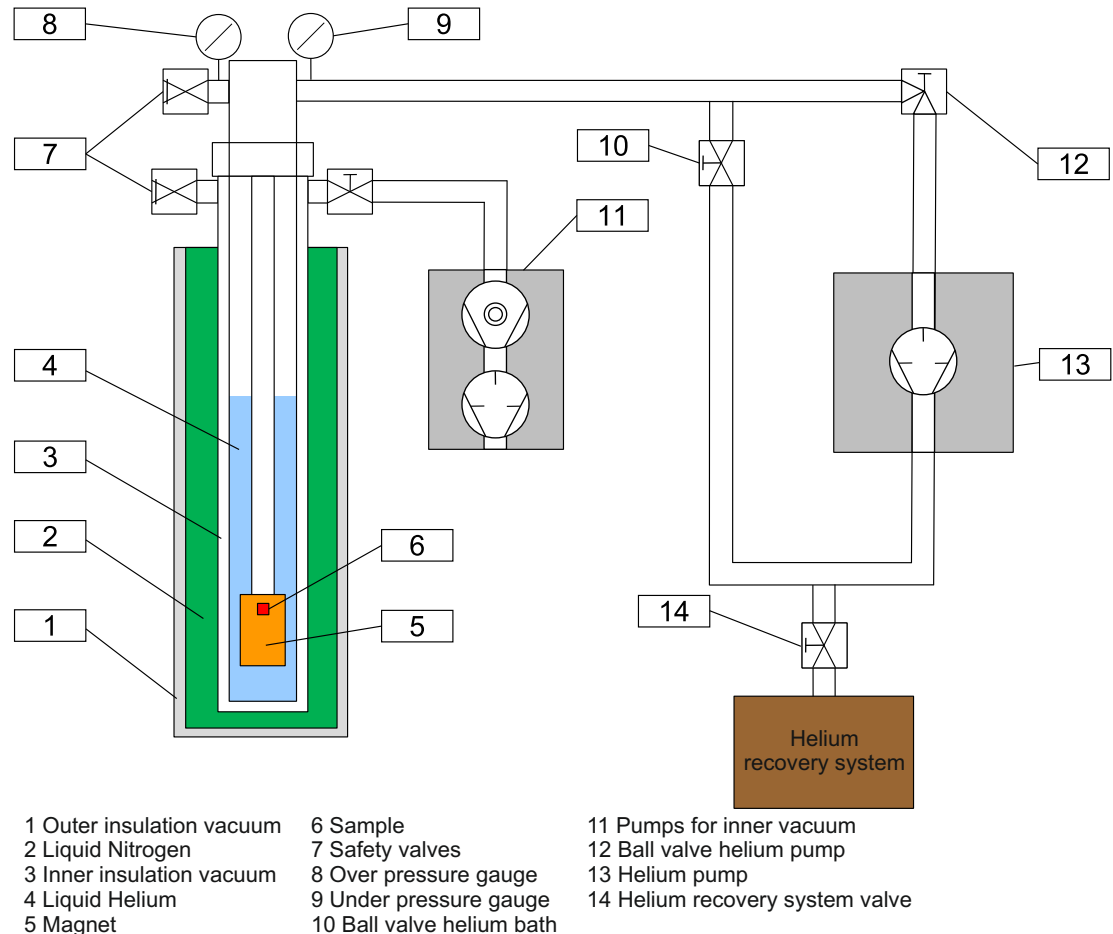


Figure 3.2: Schematic drawing of the cryostat's components.

Chapter 4

Experiment and analysis

4.1 Cooling down the cryostat

In the beginning of the cool down process the supervisor must be present. The following steps need to be taken:

1. Switch on the turbo pump's controls and the pressure gauge.
2. Switch on the forepump and subsequently the turbo pump to evacuate the inner insulation vacuum.
3. Go and get liquid Helium (LHe) and Nitrogen (LN).
4. Connect the helium dewar to the recovery system and open the appropriate valves.
5. Transfer of LN with small dewars.
6. Close the valve to the helium recovery system on the LHe dewar. The pressure inside the LHe dewar should not rise above **200 mbar**. In case it does, compensate by opening the valve again.
7. Slowly insert the helium transfer tube in the dewar until helium gas leaves from the other end.
8. Insert the transfer tube into the cryostat.
9. Continue lowering the transfer tube into the cryostat and dewar simultaneously, until it reaches the funnel inside the cryostat. Keep an eye on the pressure!
10. Once the pressure in the dewar is approaching zero, connect the hot-water bag and keep the pressure around 100 mbar.
11. Once the helium bath is full, reconnect the dewar to the recovery line and blow off the residual pressure.
12. Extract the helium transfer tube from the cryostat and dewar. (**Use cryo-gloves!!**)

4.2 Tasks

The experiment will be conducted in the following way:

1. Cool the sample down to 4.2 K and conduct a measurement of R_{xy} and R_{xx} for magnetic fields in the range of ± 6 T. Identify the LLs using equation 2.5. Mobility and charge carrier concentration may be extracted from equations 2.27 and 2.26. Estimate the quantities during the experiment and check if they are plausible!
2. Repeat the measurement at 3.2 K and 2.2 K. In order to do so, the ball valve in the helium bath exhaust line needs to be closed, the helium pump needs to be switched on and finally the ball valve in the helium pumping line is adjusted to tune the pumping speed and thus the equilibrium temperature. Especially for 3.2 K pay attention to the under pressure gauge and use figure 4.1 to estimate a proper set-point. For 2.2 K full pumping speed is required. The drop in helium pressure reduces the cooling of the magnet's current leads. The voltage limit of the current source will be reached below 6 T, thus the range of the measurement should be reduced, for instance to ± 5.6 T. *Important: Never change the temperature at the maximum magnetic field! Reduced it to at least 3 T!*
3. Take notes on the temperature and copy the temperature log file for the day to estimate the temperature error.
4. You may find the sample dimensions in figure 3.1.
5. Further analysis of the data:
 - a) Extract n_s from the SdH oscillations at different temperatures using equation 2.22. A FFT analysis is a good way of extracting the relevant frequency in $\frac{1}{B}$. Interpolate the data first to have equidistant points. Compare your results to those generated from the Hall measurements.
 - b) Use equation 2.23 to find a value for the effective mass of the electrons in the 2DEG by exploiting the temperature dependence of the SdH oscillation's amplitude. Consult supplement 4.2 for details.
 - c) Use your value of m^* to calculate τ_q for different temperatures from the magnetic field dependence of the SdH oscillation's amplitude.
 - d) Compare the different values of τ_q and τ_{tr} .
 - e) Exploit the temperature dependence of feasible SdH oscillation's minima to extract the electrons' effective g-factor. Use equation 2.35 and plot it cleverly.
 - f) Compare your results to those from the literature!

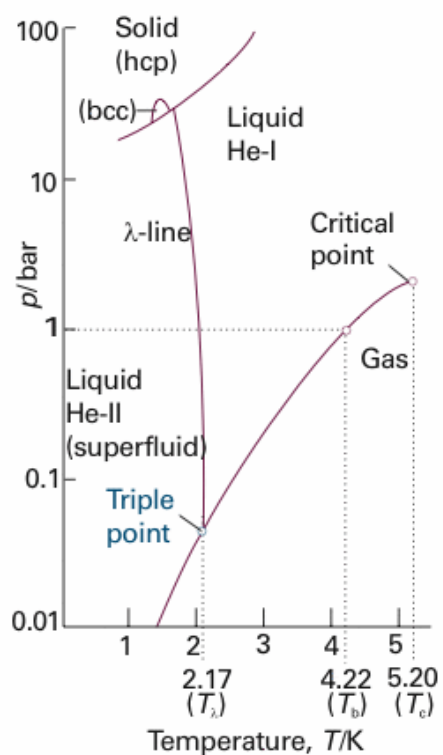


Figure 4.1: Phase diagram of ${}^4\text{He}$. [11]

Appendices

Lock-in amplifier

The detection of small electrical signals is often times very difficult, since different sources of noise will influence your signal:

- ◊ 50 Hz hum originating from the mains
- ◊ $\frac{1}{f}$ -noise of a pre-amplifier
- ◊ Thermal noise of a sensor
- ◊ Slow drift of a voltage source.
- ◊ Mobile phone radiation
- ◊ etc.

All kinds of noise sources, radiating at different frequencies, hinder usual measurement equipment to quickly find and precisely evaluate the measurement signal. AC-noise as well as DC-drift undermine the stability and accuracy of an experiment.

Whereas increased integration times help getting rid of AC-noise, at the same time it makes the measurement more susceptible to DC-drift. Additionally, it might also be either impossible or undesirable to wait very long for every data point.

Fortunately, the lock-in technique offers a possibility to get rid of high frequency noise as well as errors originating from slow voltage drifts, because integration times may be significantly reduced.

Operation principle of a lock-in amplifier

A lock-in is designed to measure a signal in a very narrow frequency range and suppress any contribution outside of it.

At first glance, this technique appears very simple. Using a band-pass filter before feeding the signal to the measurement device seldom yields the desired results. Noise suppression, speed and accuracy of a good lock-in outperform simple signal filtering techniques by orders of magnitude.

Lock-ins are able to measure tiny AC-signals, even though they might be obscured by larger noise components. The key figure is the maximum signal to noise ratio (SNR),

which a lock-in will tolerate without going astray by more than 5%. It is called *dynamic reserve* and usually one will find values of 60 dB or even 100 dB in specialized devices. Latter corresponds to a huge factor of 10^5 .

In order to perform this well, the lock-in needs to receive a very clean reference signal with the same frequency as the measurement signal. For measurements, which usually use DC-signals, one defects to low frequency ($f < 100$ Hz) AC-signals.

At the core of the lock-in is a measurement technique called phase sensitive detection (PSD). The input signal is multiplied with a reference signal of known and constant amplitude, which is phase locked with the (modulated) measurement signal. The result for two sinusoidal signals reads

$$\Phi(t) = V_1 \sin(\omega_1 t) \cdot V_2 \sin(\omega_2 t + \theta) \quad (1)$$

$$= \frac{1}{2} \cdot V_1 V_2 [\cos((\omega_1 - \omega_2)t + \theta) - \cos((\omega_1 + \omega_2)t + \theta)]. \quad (2)$$

Here V_1 and V_2 are the amplitudes of the sinus functions, ω_1 and ω_2 the corresponding angular frequencies and θ is the phase difference of the first function relative to the second. The result is emphasized in figure 2. In case of identical frequency and phase (fig. 2 a) equation 1 is reduced to

$$\Phi(t) = \frac{1}{2} V_1 V_2 [\cos(0) - \cos(2\omega t)] = \frac{1}{2} V_1 V_2 - \frac{1}{2} V_1 V_2 \cos(2\omega t). \quad (3)$$

Since the reference signal's amplitude is constant, one may low-pass filter the result of the multiplication to get rid of the $2\omega t$ component and find a constant DC-voltage, which is directly proportional to the measurement signal. Any input component, which has a differing frequency from the reference signal, does not contribute to the DC-voltage. This is clear from figure 2 b), since the result for two differing frequencies is symmetric about zero and thus does not contribute to the Lock-in output after lowpass filtering.

The lowpass filtering may be represented as an integration of the signal over a time T . The output V , resulting from the signal in equation 1, will be

$$V = \frac{1}{T} \int_0^T \Phi(t) dt \quad (4)$$

$$= \frac{V_1 V_2}{2T} \left(\frac{1}{\Delta\omega} \sin(\Delta\omega t + \theta) - \frac{1}{\Sigma\omega} \sin(\Sigma\omega t + \theta) \right), \quad (5)$$

where $\Delta\omega$ represents the difference in angular frequency and $\Sigma\omega$ the sum. Most noteworthy is the $1/\Delta\omega$ dependence in the first term. All contributions from frequencies different from the reference will eventually die out with an $1/T$ dependence. However, for small $\Delta\omega$ these contributions are large and long integration is needed to reduce them sufficiently. This slows down the measurement and thus one looks for *quiet* regions in the spectral

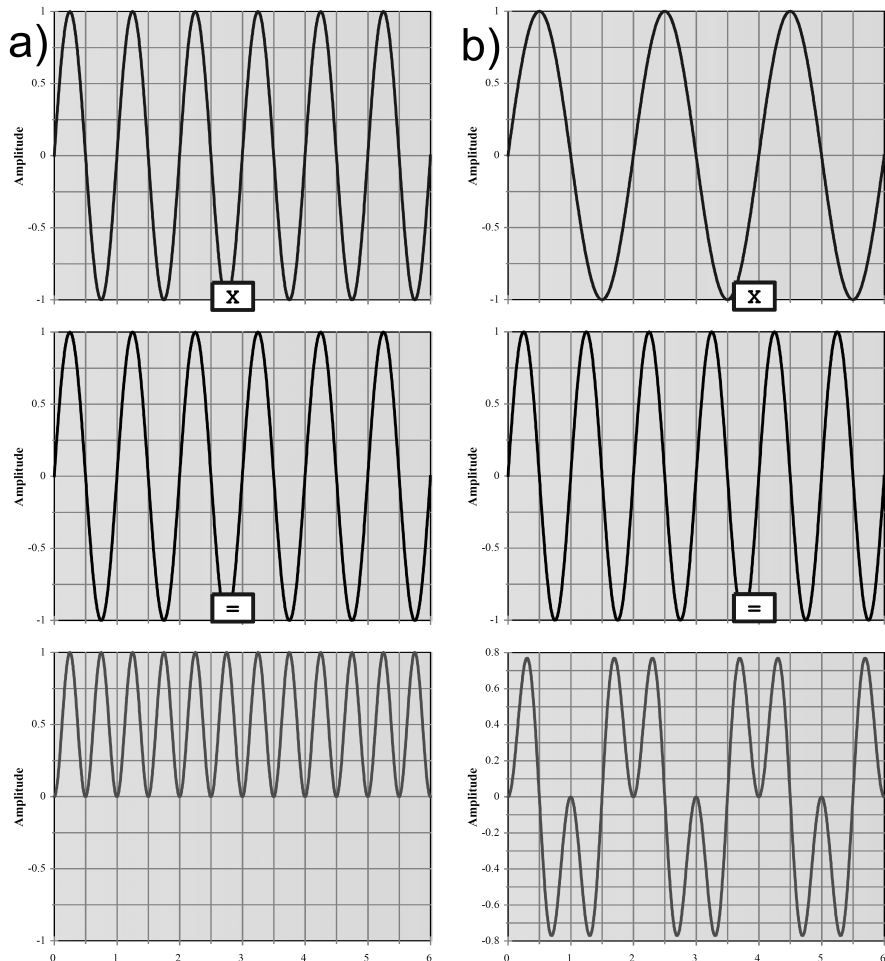


Figure 2: a) Multiplication of two phase locked sinus waves of identical frequency results in a wave with DC-contribution. b) Multiplying two sinus waves of different frequency yields a wave, which is symmetric about zero.

domain to place the reference frequency away from noise.

Looking at a DC-offset of the input signal, one realizes that the multiplication of a constant with the reference signal will also be symmetric about zero and therefore be eliminated. A slow drift of the offset will correspond to a very small frequency and will neither yield a contribution.

Signal phase

Our argumentation has so far only been precisely valid for signals which are in phase with the reference signal. The output will not match the measurement signal if there is a phase difference, but will differ by a factor of $\cos \theta$. There are two approaches to compensate for this:

- ◊ Adjust the phases to match
- ◊ Conduct a two-phase measurement

A two-phase measurement may be carried out by a one-phase lock-in by subsequently measuring with the original reference signal and then with the 90° shifted signal. The recorded values may be used to calculate the signal's amplitude and phase. However, the signal may not vary between the two measurements.

The better option is to use a two-phase lock-in. It will perform both measurements simultaneously with two independent PSD modules. One module uses the original reference sinus wave and the second uses the corresponding cosine wave. The lowpass filtered signal from the sinus-PSD is usually called X-output and the one from the cosine-PSD Y-output. For a measurement signal, which is in phase with the reference signal, the X-output will be the desired value and the Y-output will be zero. A 90° phase shift of the measurement signal will reverse the situation. One has to keep in mind that any phase shift will originate from a capacitance or inductance and needs to be discussed in terms of sensible contributions from distinguishable sources. Especially, if the phase varies during the measurement. By combining both outputs one may always calculate the total measurement signal:

$$V = \sqrt{(X^2 + Y^2)} \quad (6)$$

$$\Theta = \arctan \frac{Y}{X} \quad (7)$$

How to analyze the Shoubnikov-de Haas oscillations

On our quest to extract the effective mass we use equation 2.23:

$$\frac{R_{xx}(B)}{R_{xx}(B=0)} \approx 1 + 2 \cdot \underbrace{\cos\left(2\pi\left(\frac{E_F}{\hbar\omega_c} - \frac{1}{2}\right)\right)}_a \cdot \underbrace{\exp\left(-\frac{\pi m^*}{\tau_q e B}\right)}_b \cdot \underbrace{\frac{X}{\sinh X}}_c \cdot \underbrace{\cos\left(2\pi\left(\frac{g\mu_B B}{2\hbar\omega_c}\right)\right)}_d \quad (8)$$

with

$$X := \frac{2\pi^2 k_B T}{\hbar\omega_c}.$$

The meanings of the different terms are explained in section 2.2. The $\frac{1}{B}$ periodic oscillations in the longitudinal resistance R_{xx} are solely described by the first cosine term (a). Its value lies within the boundaries -1 and $+1$. Therefore the upper and lower envelope of the measured curves correspond to the extremal values (a) $= \pm 1$ and need to follow equations

$$\frac{R_{xx}^+(B)}{R_{xx}(B=0)} \approx 1 + 2 \cdot (+1) \cdot \exp\left(-\frac{\pi m^*}{\tau_q e B}\right) \cdot \frac{X}{\sinh X} \cdot \cos\left(2\pi\left(\frac{g\mu_B B}{2\hbar\omega_c}\right)\right) \quad (9)$$

and

$$\frac{R_{xx}^-(B)}{R_{xx}(B=0)} \approx 1 + 2 \cdot (-1) \cdot \exp\left(-\frac{\pi m^*}{\tau_q e B}\right) \cdot \frac{X}{\sinh X} \cdot \cos\left(2\pi\left(\frac{g\mu_B B}{2\hbar\omega_c}\right)\right) \quad (10)$$

for the upper and lower envelope respectively. Subtracting both equations from one another yields

$$\frac{\Delta R_{xx}^\pm(B)}{R_{xx}(B=0)} = \frac{R_{xx}^+(B) - R_{xx}^-(B)}{R_{xx}(B=0)} \approx 4 \cdot \exp\left(-\frac{\pi m^*}{\tau_q e B}\right) \cdot \frac{X}{\sinh X} \cdot \cos\left(2\pi\left(\frac{g\mu_B B}{2\hbar\omega_c}\right)\right). \quad (11)$$

The only term depending on temperature is X . Thus, dividing this equation for two different temperatures leaves a rather simple expression:

$$\frac{\Delta R_{xx}^\pm(B, T_1)}{\Delta R_{xx}^\pm(B, T_2)} \approx \frac{X(T_1) \cdot \sinh X(T_2)}{\sinh X(T_1) \cdot X(T_2)} \quad (12)$$

Further simplification gives us our final expression:

$$\frac{\Delta R_{xx}^\pm(B, T_1)}{\Delta R_{xx}^\pm(B, T_2)} \approx \frac{T_1 \cdot \sinh X(T_2)}{T_2 \cdot \sinh X(T_1)}. \quad (13)$$

If we now determine the difference of the envelopes at fixed magnetic field, but varying temperature, than the solution of the equation will give us a value for m^* . Since there is no analytical solution to the equation, one has to either find it numerically (Matlab, Maple,...) or graphically.

Comment: If the numerical route is to be taken, one should consider directly extracting the factor $x = \frac{m^*}{m_e}$, because one might encounter problems due to too high exponents during the iterations otherwise.

In order to determine the quantum relaxation time, one uses the extracted value for m^* and the rewritten equation 11, now reading

$$\ln(A \cdot \Delta R_{xx}^\pm(T, B)) = -\frac{\pi m^*}{e\tau_q} \cdot \frac{1}{B}. \quad (14)$$

If one now plots the logarithm over $\frac{1}{B}$, one may extract a value for the quantum relaxation time from the slope.

Bibliography

- [1] Harald Ibach and Hans Lüth. *Festkörperphysik Einführung in die Grundlagen von Harald Ibach, Hans Lüth.* Springer-Lehrbuch. Springer Berlin Heidelberg, Berlin, Heidelberg, 7 edition, 2009. Cited on page 9.
- [2] Thomas Ihn. *Semiconductor nanostructures : quantum states and electronic transport.* Oxford University Press, Oxford ; New York, 2010. Cited on pages 9 and 25.
- [3] D. S. Lee, V. Skakalova, R. T. Weitz, K. von Klitzing, and J. H. Smet. Transconductance fluctuations as a probe for interaction-induced quantum hall states in graphene. *Physical Review Letters*, 109(5), 2012. Cited on page 14.
- [4] S. Ilani, J. Martin, E. Teitelbaum, J. H. Smet, D. Mahalu, V. Umansky, and A. Yacoby. The microscopic nature of localization in the quantum hall effect. *Nature*, 427(6972):328–332, 2004. Cited on page 14.
- [5] Thorsten Demel. *Ein- und nulldimensionale elektronische Systeme in AlGaAs-GaAs-Heterostrukturen vorgelegt von Thorsten Demel.* MPI für Festkörperforschung, Stuttgart, 1990. Cited on page 15.
- [6] Charles Kittel. *Einführung in die Festkörperphysik mit 60 Tabellen und 134 Aufgaben* Charles Kittel. Oldenbourg, München [u.a.], 9., verb. aufl. edition, 1991. Cited on page 18.
- [7] G. Ebert. *Magnetotransportuntersuchungen an GaAs-AlGaAs-Heterostrukturen.* TU München, 1983. Cited on page 20.
- [8] K. Hashimoto, C. Sohrmann, J. Wiebe, T. Inaoka, F. Meier, Y. Hirayama, R. A. Romer, R. Wiesendanger, and M. Morgenstern. Quantum hall transition in real space: From localized to extended states. *Physical Review Letters*, 101(25), 2008. Cited on page 20.
- [9] C. W. J. Beenakker and H. Vanhouten. Quantum transport in semiconductor nanostructures. *Solid State Physics-Advances in Research and Applications*, 44:1–228, 1991. Cited on pages 21 and 23.
- [10] J. Nieder. *Magnetotransportuntersuchungen an eindimensionalen Transitoren.* MPI für Festkörperforschung, Stuttgart, 1992. Cited on page 22.

- [11] M. Mombourquette. Phase diagram ${}^4\text{he}$, 2012. Cited on page 35.